DGEN Aeropropulsion Research Turbofan Core/Combustor-Noise Measurements — Experiment and Modal Structure at Core-Nozzle Exit

Devin K. Boyle[1]
email: devin.k.boyle@nasa.gov

Brenda S. Henderson
email: brenda.s.henderson@nasa.gov

Lennart S. Hultgren[1]
email: hultgren@nasa.gov

National Aeronautics and Space Administration
Glenn Research Center
Cleveland, Ohio 44135, USA

Data from a recent core/combustor-noise source-diagnostic test utilizing a small turbofan engine are analyzed. The campaign continued the exploration begun in a baseline test, but with more extensive acoustic instrumentation. Both tests were aimed at developing a better understanding of propulsion-noise sources and their impact on the farfield noise signature, in order to enable improved turbofan noise-prediction methods and noise-mitigation techniques. Simultaneous high-data-rate acoustic measurements (93 channels in total) were obtained using a circumferential sensor array at the core-nozzle exit in conjunction with sideline and farfield microphone arrays for several relevant engine operational points. Measurements were repeated for different circumferential and sideline array configurations, as well as for redundancy. The unsteady pressure field at the core-nozzle exit is documented in detail. Previous work suggested that the ±1 azimuthal duct mode could be cut-on at this location, which would have implications for combustor-noise modeling and prediction. The modal decomposition of the combustor noise at the core-nozzle exit verifies this observation. Select farfield sound-pressure-level spectra are also presented.

Keywords: Aeroacoustics, Turbomachinery Noise, Combustor Noise

Introduction

Turbofan noise has contributions from the fan, jet and core-noise sources such as the combustor, compressor and turbine. The relative, as well as absolute, strengths of these sources have changed over time. Figure 1 is a schematic illustration[2] of the evolution of the propulsion-noise sources from early to advanced modern turbofans. For contemporary turbofan-engine designs, fan noise is, in general, the dominating propulsion-noise component, but core/combustor noise can make a significant contribution to the aft-quadrant overall noise signature at low-power conditions, typical of approach.

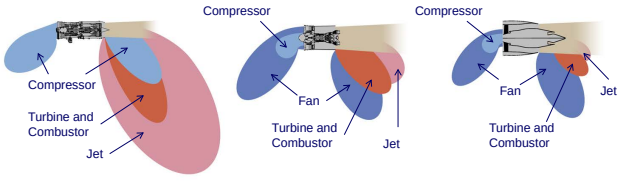

Fig. 1 Evolution of propulsion-noise sources over time; Pratt & Whitney, used with permission

Compared to current-generation turbofans, propulsion systems for future ultra-efficient commercial subsonic air vehicles are projected to be of increasingly higher bypass ratios from larger fans combined with much smaller cores, with ultra-clean burning fuel-flexible combustors [1]. These trends are expected to lead to a significant reduction in jet noise and, when combined with advances in noise mitigation, also to a substantial lessening of fan noise. However, future lean-lean combustors will operate at higher pressures and conceivably at a higher level of unsteadiness (compared to traditional rich-lean aircraft combustors), with both factors implying a strengthening of the combustor-noise sources. The envisioned reduction in turbine stages, each with a lowered blade count (less solidity), could also lessen turbine attenuation of the combustor-noise components. In addition, the higher loading of the turbine stages, in particular the first high-pressure-turbine stage, could also increase the effectiveness of the indirect combustor-noise mechanism. To summarize: *While other propulsion-noise sources can be expected to decrease in strength in the future, combustor-noise sources could show the opposite trend.* Consequently, far-term commercial-turbofan designs may well expose core-noise sources currently masked by fan and jet noise. Unless effective noise-reduction strategies are developed, combustor noise is likely to become a prominent contributor to overall airport community noise. Conceivably, it could even negate (or limit the effectiveness of) noise-mitigation advances for other propulsion noise sources. The noise/environmental impact is an issue of great importance not only to future gas-turbine propulsors, but also to proposed far-term hybrid-electric aircraft-propulsion systems.

The recent review article by Tam et al. [2] discusses experimental, theoretical, and computational combustor-noise investigations spanning the period from the 1970s through the latter part of the last decade. In particular, the review paper [2, Sections 1, 2.3, and 3.3] lists other relevant review papers, discusses experimental combustor-noise investigations utilizing real combustors in rigs or actual engines prior to the year 2000 as well as engine-noise experiments from the last two decades. The reader is encouraged to consult the references therein for more details than are given here.

There are inherent complications such as costs, safety, and facility requirements associated with real-engine tests. In general,

[1] Corresponding author
[2] From Epstein, A., Invited Lecture, *ISABE*, Phoenix, Arizona, 2015

aircraft-engine manufacturers also consider their acoustic data as proprietary. As a consequence, only a limited number of recent engine-acoustics investigations are available in the open literature. These were generally carried out with government support or directly by government research organizations.

A significant difficulty in determining the core/combustor-noise contribution to the farfield noise signature of a real turbofan is that an engine has many noise sources. In particular, jet noise can mask the core/combustor-noise under static-engine tests even when it would not do so during flight. Mendoza et al. [3] and Hultgren and Miles [4] evaluated source-separation techniques to determine the combustor-noise contribution to the overall noise signature of the Honeywell TECH977 research turbofan engine (typical of business-jet propulsion systems) using data obtained during the NASA/Honeywell EVNERT program [5]. The acoustic measurements were obtained using an outdoor static-engine test facility, with ground-based microphones in the geometric farfield, and engine-internal unsteady pressure sensors.

Other relevant core/combustor-noise results obtained by analyzing EVNERT data are presented by Royalty and Schuster [6], Miles [7], and Hultgren [8]. Royalty and Schuster [6] documented the modal structure of the unsteady pressure field in the non-premixed combustor of the TECH977 research turbofan. Miles [7] demonstrated the separation of direct and indirect contributions to the combustor noise by using a coherence technique, involving a combustor-internal pressure sensor and farfield microphones, and examining the time delay between the coherent signals. He found that the cross-spectral frequency band 0-200 Hz was dominated by indirect combustion noise generated by entropy waves interacting with the turbine, but attributed the coherent signal in the dominant 200–400 Hz frequency range mainly to direct combustion noise. Hultgren [8] used a coherence method involving three engine-internal unsteady pressure sensors to determine the turbine-transfer function for direct combustor noise.

Harper-Bourne et al. [9] presented a combustor-noise investigation of the European ANTLE turbofan demonstrator engine. This engine is a large, high-bypass, three-spool turbofan derived from the Rolls-Royce Trent 500 engine (which powers the twin-aisle Airbus A340/500-600 aircraft). The acoustic testing took place in an indoor test cell and involved engine-internal unsteady pressure sensors as well as engine-external microphones. The microphones were placed at the intersection of the test-cell floor and (vertical) walls and can be considered as being in the acoustic field, but not in the geometric farfield. Cross-correlation and impulse-response methods were applied to determine the combustor noise.

Pardowitz et al. [10] analyzed comprehensive acoustic measurements inside and outside of a turboshaft engine (Ardiden 1H-1 helicopter engine). The extensive instrumentation included sensors in the combustor chamber, downstream of the high-pressure turbine, between the stages of the two-stage power turbine, and in the exhaust nozzle, as well as geometric-farfield microphones. The application of coherence techniques, including the first application to real-engine data of advanced approaches that combine correlation methods and mode decomposition techniques [11], allowed the quantification of the different noise-source contributions to the total sound power as well as the impact of various core-noise sources in different frequency bands.

Schuster et al. [12] successfully measured engine-internal temperature and pressure fluctuations relevant to core/combustor noise during a NASA funded test campaign [13] using the Honeywell TECH977 research turbofan. The hostile environment inside an engine combustor makes the measurement of unsteady temperatures over a sufficiently large frequency range particularly difficult. This study is one of the first, if not the very first, available in the open literature where this has been achieved. Tam et al. [14] provided a computational model for and a further discussion of these results.

The NASA core/combustor-noise research efforts are aimed at obtaining a better understanding of propulsion-noise sources (in particular those associated with the combustor) and their impact on the farfield noise signature. The ultimate goal is to enable improved turbofan noise-prediction methods as well as noise-mitigation techniques. This paper describes and presents results from the July–August 2019 DGEN Aeropropulsion Research Turbofan (DART) source-diagnostic test (SDT) carried out at the NASA Glenn Research Center (GRC) in the Aero-Acoustic Propulsion Laboratory (AAPL).[3] The 2019-SDT campaign continued the exploration and documentation of the DART core/combustor noise begun with a 2017 baseline test [15]. This earlier test was also performed in the NASA GRC AAPL facility. The 2017 test provided a baseline data set that included measurements at the core-nozzle exit via two infinite-tube-probe (ITP) [16–19] unsteady-pressure sensors. Additionally, a single midfield microphone and a farfield (overhead) microphone array were used at that time. Among the findings [15] was the indication that the ±1 azimuthal duct mode likely was cut-on at the core-nozzle exit, which has implications for the combustor noise emanating from the engine and modeling and prediction thereof.

The 2019-SDT campaign utilized a significantly expanded sensor suite compared to the 2017 test. In total, 93 simultaneously sampled sensors were used for high-rate acoustic-data acquisition. An 8-ITP circumferential array at the core-nozzle exit in conjunction with 61-microphone-sideline and 24-microphone-farfield arrays were employed. The resulting extensive data set will allow for the application of advanced source-separation and phased-array methods to elucidate not only the core-noise structure, but also the propagation characteristics of other propulsion noise sources. The present paper concentrates on documenting the modal structure of the combustor noise emanating from the engine, however. A detailed core-nozzle-exit noise survey based on the circumferential-array measurements is presented. Sound-pressure-level (*SPL*) spectra from select sideline and farfield measurement locations of interest to core-noise evaluation are also discussed.

Experimental Setup

The 2019-SDT campaign took place within the AAPL facility at NASA GRC, which is a hemispheric dome with a radius of about 20 m (65 ft) and acoustic treatment on the walls and floor. The treatment consists of fiberglass wedges, with a 0.61 m (2 ft) depth, resulting in an anechoic limit of approximately 150 Hz. The DART was positioned near the center of the facility allowing the use of the existing AAPL overhead microphone-array superstructure. Figure 2 shows the DART and microphone arrays in AAPL. During normal operation the door on the far right is open to allow engine exhaust to exit the facility. The coordinate system used to describe measurement locations is a spherical one with its origin located on the engine centerline at the core-nozzle exit plane. The polar angle is zero in the inlet direction and the azimuthal angle is zero in the engine port-side (left-hand side facing forward) horizontal plane.

DGEN Aeropropulsion Research Turbofan. DART is a cost-efficient testbed for the study of core-noise physics and mitigation. The kernel of this resource is an AKIRA MecaTurbines DGEN 380 turbofan engine.[4] It is a two-spool 500 lbf (2.2 kN) thrust-class geared turbofan engine with a bypass ratio of approximately 7.6. The single stage fan rotor contains 14 wide-chord blades and is geared to the low-pressure shaft at a ratio of 3.32. A single stage axial uncooled low-pressure turbine drives the fan gearbox. The high-pressure centrifugal compressor is driven by a single stage axial uncooled high-pressure turbine. Jet-A fuel (kerosene) is burned in a conventional reverse-flow annular combustor. Its modular design allows the replacement of major components with parts modified for invasive instrumentation with comparative ease. Even though it is a rather small turbofan engine, its acoustic signature is relevant to large commercial aircraft engines [20, 21].

[3] This test will be referred to as 2019 SDT herein.

[4] Originally developed by Price Induction for the personal-light-jet market.

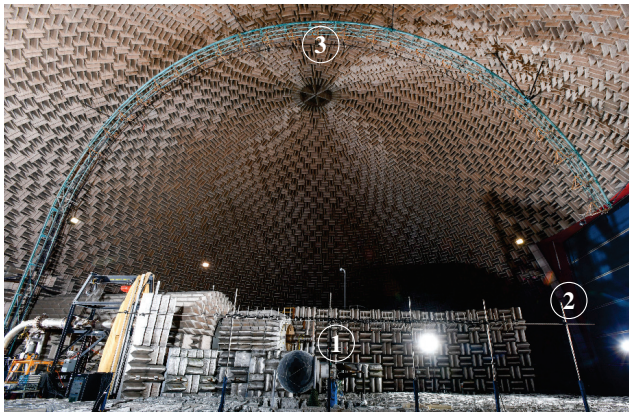

Fig. 2 DART ①, sideline ② and overhead ③ arrays

Farfield (Overhead) Microphone Array. The 24 microphone locations of the AAPL overhead array were used in this test, see ③ in Fig. 2. Each microphone was aimed at the center of the core-exhaust plane. The microphone polar angles, relative to the engine center axis, fall in the approximate range of 42–150 °. Note that both the azimuthal angle and the radial distance vary with the microphone polar angle since the 'design origin' of the overhead array is fixed within the AAPL and does not coincide with the origin used here. Due to the out of azimuthal-plane rotation of the overhead array, the azimuthal angles fall in a range of about 84–118 °. The radial distance ranged between 48–74 core-nozzle diameters. The overhead-array microphones can, hence, be considered to be in the geometric farfield.

The overhead-array microphones are referred to as sensors FF001 through FF024, with the 'FF' implying geometric farfield and the numerical index increasing with aft location. The array is populated with Brüel & Kjær type 4939 1/4-inch (6-mm) externally-polarized freefield microphones.

Linear Sideline Microphone Array. In addition to the microphones mounted in the overhead array, a sideline microphone array was also utilized. Since it was desired to acquire data simultaneously for the overhead and sideline arrays, the preferable ground-plane-microphone hard-surface arrangement for the latter could not be used. In that case, reflections from the hard-surface floor would have interfered with the overhead geometric-farfield measurements. The microphones were consequently pole mounted, with their faces pointed at, and perpendicular to, the engine centerline axis. The AAPL floor was covered with acoustic wedges.

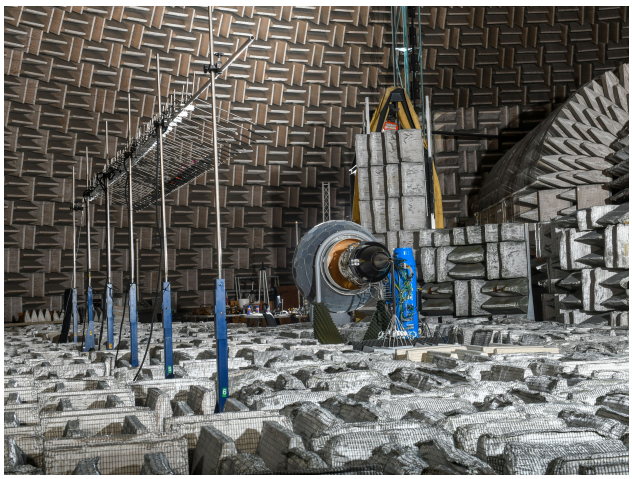

Fig. 3 DART turbofan and sideline array

The sideline array was designed to have a nominal 2.24-m (88-inch) horizontal offset from the engine-center axis and a nominal (polar) aperture of 30–150 °, with a varying microphone spacing to achieve a constant two-degree polar-angle separation. A previous investigation of the anechoic properties of the acoustic wedges in AAPL[5] had shown that a glancing angle of less than 30 ° leads to unacceptable 'ground' reflections. This constraint, in combination with the desired array aperture, implied that the sideline array also needed a positive vertical offset from the engine center-line height. The final-design vertical offset was chosen such that the microphone faces nominally would be perpendicular to the 22.25 ° azimuthal direction. The actual polar aperture and azimuthal angle of the array, as measured after assembly, turned out to be 31–147 ° and 22.0 ± 0.6 °, respectively. Figure 3 offers a perspective of the sideline array and engine.[6]

The 61 sideline-array microphones are labeled as sensors SL101 through SL161, with the 'SL' indicating sideline and the numerical part increasing in the fore-to-aft direction. The forward 30 microphones were PCB® model 378C01 and the remaining 31 microphones were GRAS type 46BE. Both types are pre-polarized 1/4-inch (6-mm) freefield microphones.

Core-Nozzle-Exit (On-Engine) Circumferential ITP Array. Eight ITPs, each instrumented with a Kulite® XCS-190-5D 5 psi (34.47 kPa) differential unsteady pressure transducer vented to atmospheric pressure, were installed at the core-nozzle exit providing engine-internal measurements. This was implemented by replacing the standard tailcone, that also serves as the inner wall of the downstream portion of the annular core-nozzle, with a modified tailcone having a circumferential array of eight static pressure ports, see Fig. 4.[7] The ITP ports are located approximately 25.4 mm (1 inch) upstream of the core nozzle exit plane and are uniformly spaced. Note that a single circumferential array cannot distinguish between upstream and downstream propagating modes.

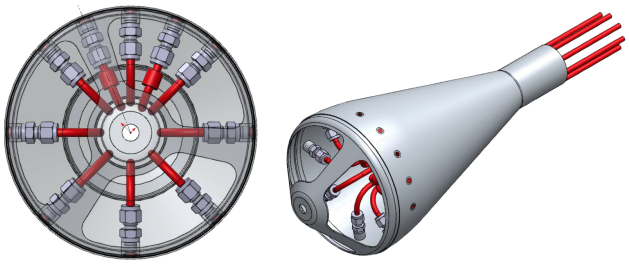

Fig. 4 Schematic of modified DART tailcone with ports for eight equally spaced ITP lines

Each ITP consists of a sense line, a transducer tee, and an "infinite" line beyond the transducer. The sense line is a wave guide transmitting unsteady pressure waves to the transducer, which is teed into the line in a way that minimizes volume changes and discontinuities. The continued line was sufficiently long to attenuate any reflections from its termination. More details of ITP configuration can be found in Boyle et al. [19].

The sense lines are connected to the eight static-pressure ports, routed through the hollow interior of the tailcone, bundled together and brought across the core and fan streams inside a symmetrical-airfoil-shaped steel channel, and finally connected to the transducer tees beyond the streams, see Fig. 5. The symmetric airfoil conduit is used in order to minimize any extraneous noise sources introduced by the sense lines traversing the jet flows.

[5] Bozak, R. F., Private Communication, 2019

[6] An alternate similarly-designed sideline array was also employed in the experiment, but will not be discussed in detail herein; it was placed at a horizontal offset of 27.6 m (148 inch), but had a smaller aperture of about 45–135 °

[7] This schematic also shows two additional instrumentation ports

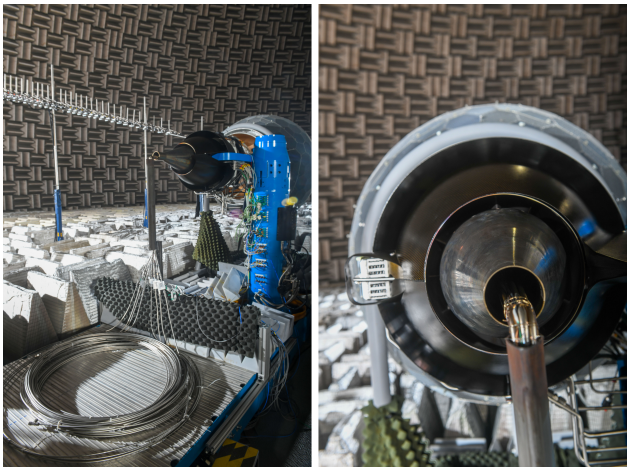

Fig. 5 Modified tailcone installed on DART

For the 2019-SDT campaign, it was decided to use a nominal 1/4-inch (6.35 mm) outer diameter line for the entire ITP. A sense line diameter as large as this is uncommon in many turbofan-engine applications, but is appropriate for a core/combustor-noise focus where the frequencies of interest are low enough to avoid having higher-order acoustic modes also propagating in the line. The obvious benefit is that amplitude and phase corrections in the transfer function are much lower than for smaller line diameters where viscous dissipation is greater. The stainless-steel sense lines were 1.22 m (48 inch) long. A custom tee design was implemented in which the line passed through a 12.7 mm (1/2 inch) aluminum block. The block itself was drilled and tapped for the Kulite® transducers, placing the transducer face flush with the inner wall of the sense line. A 15.24 m (50 ft) stainless-steel coil was attached to the other side of the tee and terminated with a hard-wall end cap.

The ITP sensors are labeled NE801 through NE808, with the 'NE' indicating (core) nozzle exit. The standard location for sensor port NE801 is in the twelve o'clock (90 ° azimuthal) position. The sensor numerical index increases in the positive azimuthal direction (clockwise direction from back of engine looking forward). The circumferential array is also used in a 'clocked' position where the modified tailcone is rotated 22.5 ° in the counter-clockwise direction. In this configuration, the NE801 port is in the 67.5 ° azimuthal position.

Data Acquisition. For the research data, a PXIe-1082 National Instruments™ (NI) chassis equipped with PXIe-4498/4499 24-bit analog-to-digital modules was used. The chassis, controlled by NI LabVIEW, simultaneously recorded 93 channels of acoustic data at each test point with a rate of 100,000 samples per second for 60 s. Prior to each acquisition, gains were set based on exposure to 20 s of steady-state engine operation. The program output time histories in physical units to disk. Each individual series contains just over 6 million points, i.e. over 558 million data points were obtained for each test condition. Additionally, ensemble-averaged power spectra were output from the NI-LabVIEW program controlling the acquisition for verification of test-point data quality during the test as well as for comparison with results from post-processing routines.

Time series data were analyzed post-test using MATLAB® scripts and routines. In general auto-spectra and cross-spectra are computed as in [15] using a data-segment length of 16,384 points (corresponding to a frequency resolution, or binwidth, of 6.1 Hz), Hamming windowing, and a 50% data-segment overlap. The resulting narrowband spectra are the average of a very large number of realizations (typically 733 instantaneous spectra).

In addition, a DART-integral engine-data system recorded select mean-line data—such as ambient conditions, turbofan engine-station data, and engine-performance parameters—at a sampling rate of 1 Hz.

Test Points and Engine Operation. The full authority digital engine controller (FADEC) of the DART commands engine power settings using the corrected low-pressure-shaft speed,

$$N_{\mathrm{Lc}} = N_{\mathrm{L}} \sqrt{\frac{T_{\mathrm{SLS}}}{T_{\mathrm{amb}}}} \,, \tag{1}$$

where N_{L}, T_{SLS}, and T_{amb} are the actual low-pressure-shaft speed, the sea-level standard temperature (288.15 K), and the ambient temperature.

Engine operation is controlled through the DART-integral engine-data system. It consists of a National Instruments™ chassis executing a LabVIEW software program. The control program starts at ground idle (33%) and then sequences through the engine-power settings of 50%, 60%, 70%, 80%, 90% and a temperature-dependent maximum, dwelling at each for 120 s (including the ground idle point). Normally, the 7-point sequence is immediately repeated once for redundancy. Engine set-point repeatability is excellent as demonstrated earlier in Boyle et al. [15]. The maximum power setting varied between test days as well as time of day because of its dependency on the ambient temperature, but this set point is not as valuable to core/combustor-noise research due to the dominance of aft-fan and jet noise sources at full power. Additionally, background measurements were collected with the engine shut down and auxiliary systems running (fuel pump, oil pump, etc.).

Overall, there were a total of six major test configurations. For each of the two sideline-array locations,[8] the modified tailcone was oriented in its standard and clocked positions and an unmodified tailcone without pressure ports was also used.

Uncertainty and Error Estimates

For a well-designed instrumentation chain, the factors generally dominating the overall uncertainty and error in the measurements are the accuracy of calibrations and the proper application of potential correction factors such as those due to the sound-field incidence angle on microphones and the ITP design.

The estimates developed below are based on calibration reports from the NASA GRC Calibration Laboratory and documentation readily available on the manufacturer's websites, as well as previous work [19]. Unless otherwise specified, they are developed for frequencies up to 10 kHz, with a lower limit of 150 Hz for the microphone measurements.

Microphone-Measurement Estimates. The microphones are of the free-field type, which are designed to measure the sound field as it would be in the absence of the microphone. At higher frequencies, the local sound pressure is affected by the microphone presence, however. The manufacturers provide corrections to compensate for this local-sound-field distortion and calibration facilities apply these when determining the microphone sound-field frequency response (normally at zero-incidence angle) relative to that at 250 Hz. The microphone sensitivity, i.e. its response at 250 Hz, is then determined (re-calibrated) in situ. The relevant factors then are: the accuracy of the piston phone used to calibrate the sensitivity, the uncertainty in the sound-field response of the microphone as a function of frequency and incidence angle of the sound wave, as well as uncertainty in the incidence angle itself.

The GRAS AP42 Class-0 piston phone used for in-situ sensitivity calibration has an accuracy/uncertainty of ±0.1 dB. Typically, the B&K and GRAS microphones both have sound-field response uncertainties not exceeding 0.16 dB, whereas the corresponding value for a PCB® microphone is 0.32 dB. Based on the

[8] Alternate-location-array (further-offset) data will be reported in the near future

data sheet for the GRAS microphone used, it can be observed that at 10 kHz the incidence-angle effect is rather gradual and in total does not exceed about 1.5 dB. For less than 2 kHz, there is no significant effect. An uncertainty of about 1–2° in the physical orientation of a microphone face, consequently, has no significant effect on the overall uncertainty of microphone measurements up to 10 kHz. Consequently, the overall uncertainty in the measurements is ±0.3 dB for the B&K and GRAS microphones and ±0.4 dB for the PCB® microphones.

At zero-incidence angle, not accounting for the sound-field frequency response results in an error less than ±0.1 dB, ±0.45 dB, and ±0.13 dB for the B&K, GRAS, and PCB® microphones, respectively.

The overhead-array microphones are in the geometric farfield and were oriented to point at the source region of the core/combustor noise in order to minimize, if not fully remove, the incidence-angle effect. However, the GRAS and PCB® microphones used in the sideline array are pointed perpendicular to the engine centerline axis and not at the core-nozzle exit. For frequencies above about 2 kHz, an incidence-angle correction should be applied to the measurements. If not, as presently, the sound field could be overpredicted by as much as 1 dB at 10 kHz.

ITP-Kulite®-Measurement Estimates. Static pressure taps on duct walls are normally considered as minimally intrusive, particularly at the low frequencies of interest to combustor noise. Pressure sensors, such as the Kulite® used here, are normally calibrated statically, namely a sequence of accurately known pressures are applied and the corresponding sensor voltages are recorded by the calibration facility. The transducer sensitivity is simply the slope of the resulting linear curve fit to the calibration data.

From the calibration reports, it is concluded here that the sensor-sensitivity uncertainty falls in the range of 0.3–0.8%. The lower number is a statistical uncertainty estimate from the linear-regression method used to obtain the sensitivity (slope) and the higher number is simply the largest relative uncertainty of the voltage measurements. Using the larger of these two numbers, the measurement uncertainty associated with the transducer sensitivity under static loading is less than ±0.07 dB. Section 3 in the Kulite Pressure Transducer Handbook,[9] states that the transducer can be considered as a second-order single-degree of freedom system with a damping factor less than 0.02. Since the resonance frequency for the transducers used is 150 kHz, it turns out that at 10 kHz the fluctuating pressure would be overpredicted by 0.45%, which corresponds to 0.04 dB. At 3 kHz, the corresponding estimates would be 0.04% and 0.004 dB – a truly insignificant error. A reasonable estimate of the sensor uncertainty is thus ±0.1 dB.

Boyle et al. [19, Fig. 11] shows that the error caused by using the ideal ITP transfer function rather than an experimentally determined one is less than about ±0.25 dB for the design used here. If no ITP corrections are applied, the fluctuating pressures will be underpredicted by several dB. However, for a coherence-based method where an ITP provides the reference signal, this magnitude reduction is actually canceled out. Only the time delay, or phase lag, which is well described by the ideal ITP transfer function, may need to be accounted for in this latter case.

Potential Acoustic-Field Contamination. The ITP sense lines (see Fig. 5) are contained within a symmetric airfoil as they cross the core and fan streams to minimize vortex shedding. Still, blunt-body vortex shedding and the impact of shear-layer turbulence on the airfoil could potentially contaminate the external acoustic field. The estimated blunt-body shedding frequencies based on the cord length fall in the ranges of 300–600 Hz and 180–370 Hz for the core and fan streams, respectively, depending on power setting. The test matrix contains complementary entries with an uninstrumented tailcone in order to document the potential effects of the ITP-sense-line routing on the farfield and sideline acoustic measurements. No discrete tones associated with vortex shedding, nor any impact of shear-layer turbulence impinging on the airfoil, have been identified in processed data from this test to date.

[9] https://kulite.com/technology/reference-library/ – Retrieved January 29, 2020

Table 1 Typical values for select shaft- and blade-passing tones [15]

$\%N_{Lc}$	SPF_H, Hz	SPF_L, Hz	SPF_F, Hz	BPF_L, Hz	BPF_F, Hz
33	453	244	73	9,256	1,027
50	611	370	112	14,069	1,561
60	681	444	134	16,884	1,874
70	739	518	156	19,701	2,186
80	787	593	179	22,518	2,499
90	831	667	201	25,332	2,811
92.5	842	685	206	26,022	2,888

Results

This two-spool geared turbofan has a number of tones expected to be visible in the spectra. Table 1, adopted from Boyle et al. [15, Table 3], lists typical shaft-passing frequencies for the high-pressure spool (SPF_H), the low-pressure spool (SPF_L), and the fan (SPF_F), as well as blade-passing frequencies for the fan (BPF_F) and low-pressure turbine (BPF_L). The values in the table correspond to test points 2–8 in the earlier work.

Data Repeatability and Quality. The 2019-SDT campaign occurred over the course of multiple days and involved several reconfigurations. Appropriate comparisons were made between results from different test days to confirm repeatability of the data. It was found that, due to the consistent ability of the FADEC to reach and hold the specified engine-operational points, excellent repeatability was realized. As an example, Fig. 6 shows the NE801 *SPL* at engine-idle (33%) and background (0%) conditions with the modified tailcone in the standard orientation for two different test days. The spectra corresponding to the different days closely track each other (generally within 1 dB) indicating a high level of repeatability of the results. The signal-to-noise ratio (*SNR*) displayed in this figure is also quite excellent. The *SNR* for the ITP measurements is further illustrated in Fig. 7 for the worst case scenario, namely at the engine-idle condition, by comparing all eight ITP *SPL* spectra

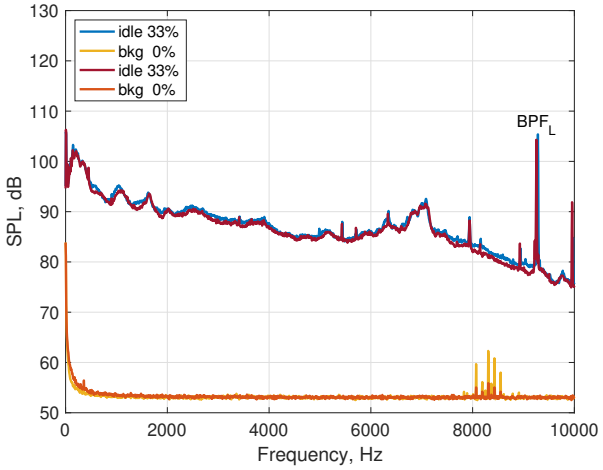

Fig. 6 ITP NE801 narrowband *SPL* at engine-idle (33% N_{Lc}) and background conditions in same configuration for two different test days—blue/yellow and red/orange pairs are for different days

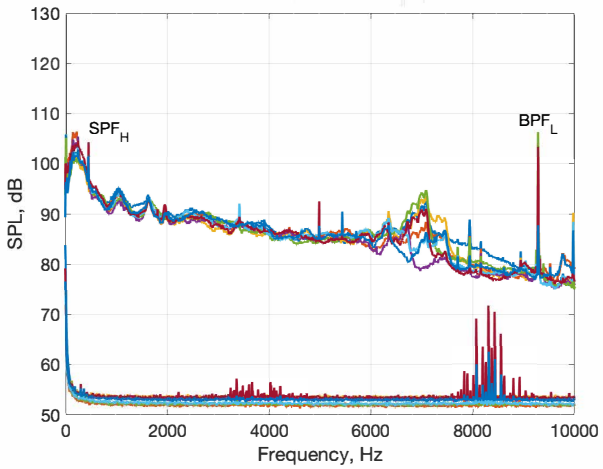

Fig. 7 ITP NE801–NE808 narrowband *SPL* at engine idle (33% N_{Lc}) and background conditions; same legend as Fig. 8

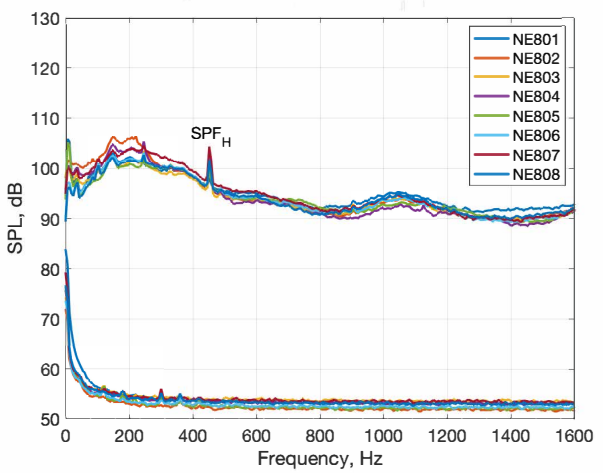

Fig. 8 ITP NE801–NE808 narrowband *SPL* at engine idle (33% N_{Lc}) and background conditions

at idle and background conditions. Aside from the region between 8–9 kHz (which is suspected to be affected by facility electronic noise) the *SNR* is quite high. All eight ITP signals trend very well with each other up to about 6 kHz. Some *SPF* and *BPF* tones are present in all the spectra as well. Figure 8 presents a closer look at the spectra in the frequency range up to 1,600 Hz, the region of interest for combustor noise. It shows broadband humps between 200–500 Hz and around 1 kHz. Additionally, the high-pressure-spool shaft-passing frequency, which is also sometimes referred to as a compressor-disk tone, is prominent in the spectra.

ITP Spectra. Circumferentially-averaged *SPL* spectra, obtained by summing mean-squared pressures, are presented in Fig. 9 for power settings between 50–90% N_{Lc}. The spread in spectral amplitudes, which is evident at lower frequencies, starts to diminish above about 8 kHz. The increase in frequency for prominent tones with power setting, i.e. rotational speed, is evident. Again, for these power settings of interest, the *SNR* is quite excellent. Figure 10 shows the averaged ITP spectra zoomed into the 0–1,600 Hz frequency range. Several *SPF* tones and harmonics can be identified. As a reminder, the only *BPF* tone occurring at a frequency low enough to potentially be observed in this range is $BPF_F \approx$ 1,561 Hz at 50% N_{Lc}. Again, a clear broadband hump appears in the spectra at all power settings between 200–500 Hz. Its peak value increases slightly slower than the overall spectra with engine power. A second broadband hump is also here visible in the spectra.

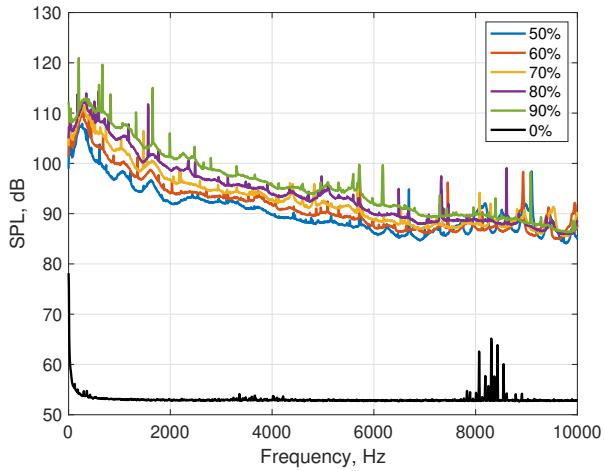

Fig. 9 Circumferentially-averaged ITP *SPL*; power settings 50–90% N_{Lc}

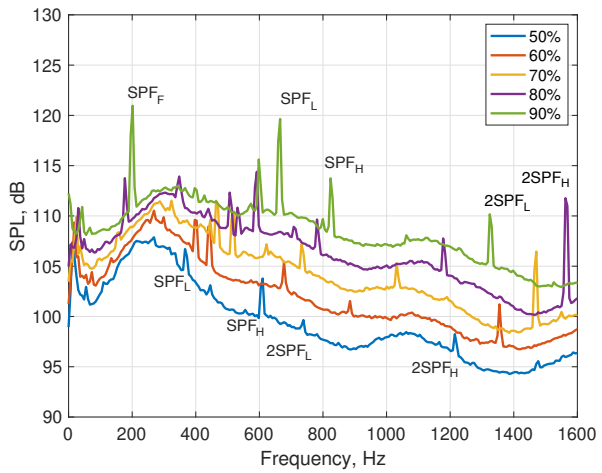

Fig. 10 Circumferentially-averaged ITP *SPL* for power settings 50–90% N_{Lc} showing more detail at frequencies below 1,600 Hz

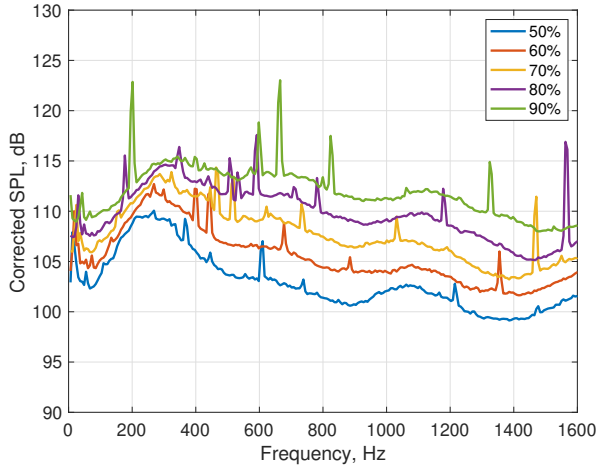

Fig. 11 Corrected circumferentially-averaged core-nozzle-exit *SPL*; power settings 50–90% N_{Lc}

Figure 11 shows the circumferentially-averaged *SPL* spectra after an ideal correction for the ITP-sense-line length has been ap-

plied. Only the transfer-function correction accounting for viscous effects in an ideal line was applied, i.e. transducer-tee-volume and finite-coil effects were ignored, see Boyle et al. [19] for details. The details of the spectra are preserved but the general falloff with increasing frequency is reduced.

Sideline- and Farfield-Array *SPL* in the 120° Polar Direction. As a relevant example from a combustor-noise perspective, the sideline- and farfield-array *SPL* spectra in roughly the 120° polar direction are shown below. The sideline and overhead microphone measurements will be discussed in detail in future reports on ongoing applications of various noise-source-separation methods to the experimental data from the 2019-SDT effort.

Sideline-Array Spectrum. Narrowband *SPL* spectra for the sideline microphone at the 121° polar angle (SL148) are shown in Fig. 12 for the background condition and power settings from 50–90% N_{Lc}. Figure 13 presents the SL148 *SPL* spectra zoomed in to the frequency range of 0–1,600 Hz in order to show the spectral characteristics and tonal content in more detail in the frequency region of interest for combustor noise. The SL148 microphone is located approximately 12.5 core-nozzle diameters from the intersection of the engine centerline and the core-nozzle exit plane.

The *SNR* (Fig. 12) is excellent for frequencies above the anechoic limit of the facility. Numerous shaft harmonics are present in the spectra. The first fan and first low-pressure-turbine blade-passing-frequencies are visible at 50% power. While the BPF_L tone appears also in ITP spectra, the BPF_F tone is only detected in the external array spectra since this turbofan engine has a dual-stream nozzle, and the ITPs only sense fluctuations in the core stream. Several higher harmonics of primarily *SPF* tones show up as well. Haystacking is observed at the second BPF_F harmonic. This behavior was previously observed by Boyle et al. [15] and appears to occur at all power settings. The spectral shape and character match well with the previous 2017-baseline test campaign [15]. Once again, the spectra exhibit a low-frequency broadband spectral hump at all power settings.

Farfield-Array Spectrum. The AAPL overhead-array microphones are all located at sufficiently large distances from the DART-defined origin to be considered as situated in the geometric farfield of sound waves emitted by the engine. Microphone FF019 is approximately 51 nozzle diameters from the core-nozzle exit and is located in the 120° polar direction. Figure 14 depicts the narrowband *SPL* spectra for microphone FF019 for power settings of 50–90% N_{Lc} as well as for the background condition.

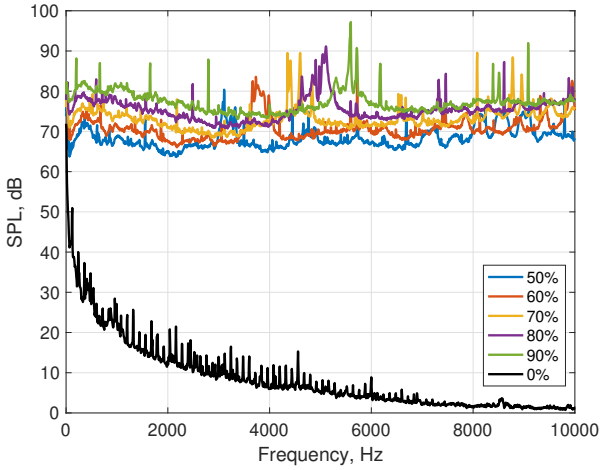

Fig. 12 Sideline microphone SL148 (121° polar angle) *SPL* for power settings 50–90% N_{Lc} and background

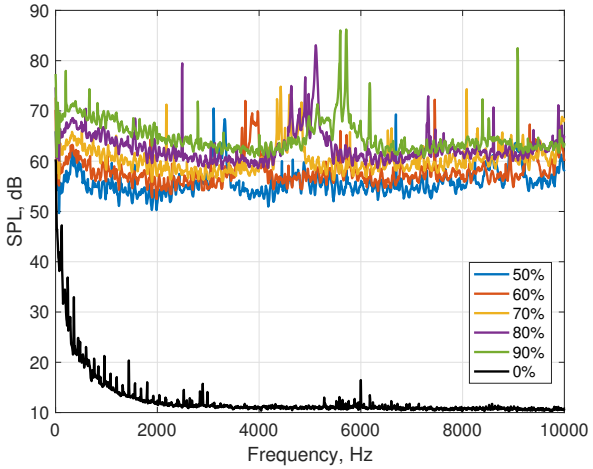

Fig. 14 Farfield microphone FF019 (120° polar angle) *SPL* for power settings 50–90% N_{Lc} and background

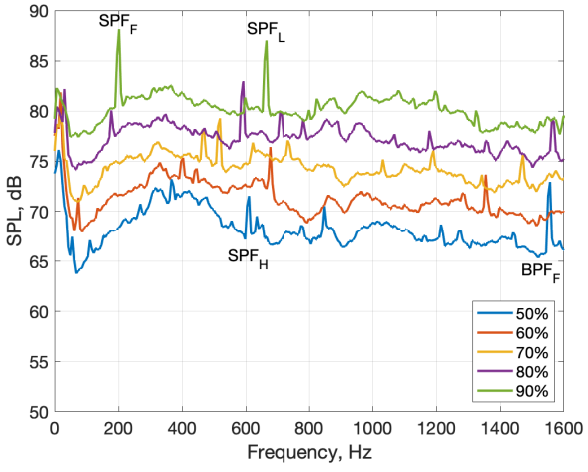

Fig. 13 Sideline microphone SL148 (121° polar angle) *SPL* for power settings 50–90% N_{Lc}; zoomed in frequency range

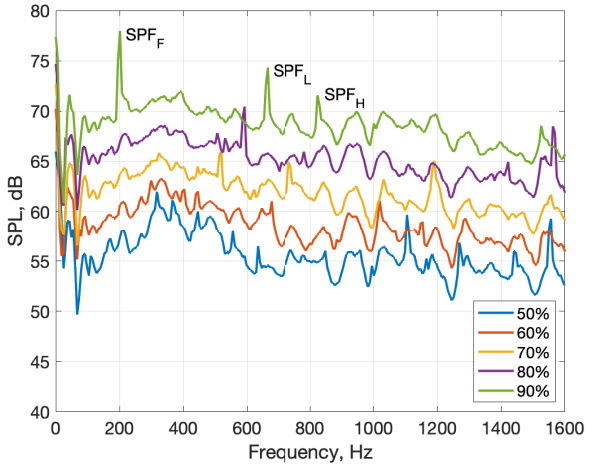

Fig. 15 Farfield microphone FF019 (120° polar angle) *SPL* for power settings from 50–90% N_{Lc}; zoomed in frequency range

Table 2 Estimated duct-mode cut-on/off frequencies (Hz) at the core-nozzle exit [15]

Power		n=0	n=1	n=2	n=3
60%	m=0	0	11,532	23,033	34,541
	m=1	793	11,559	23,047	34,550
	m=2	1,586	11,642	23,088	34,577
	m=3	2,378	11,779	23,157	34,623
70%	m=0	0	11,491	22,951	34,417
	m=1	790	11,518	22,964	34,426
	m=2	1,580	11,601	23,005	34,454
	m=3	2,370	11,738	23,074	34,500
80%	m=0	0	11,465	22,900	34,341
	m=1	789	11,493	22,913	34,350
	m=2	1,577	11,575	22,954	34,377
	m=3	2,365	11,711	23,023	34,423
90%	m=0	0	11,414	22,797	34,187
	m=1	785	11,441	22,810	34,196
	m=2	1,570	11,523	22,851	34,223
	m=3	2,355	11,659	22,919	34,268

The *SNR* margin, above the AAPL anechoic limit, again is excellent. Figure 15 gives a more detailed view at the lower frequency range of 0–1,600Hz. The overall features of the spectra are similar to the corresponding ones for the sideline-microphone SL148. The overall reduction in *SPL* levels between the two microphones is consistent with spherical spreading. The slightly more rapid falloff with frequency for the FF019 spectra is likely due to atmospheric attenuation having occurred over a longer distance. The SPF tones are also present here as well as the haystacking around the $2BPF_{\mathrm{F}}$ tone.

ITP-Array Modal Analysis

A modal decomposition of the unsteady pressure field at the core-nozzle-exit plane was performed utilizing data acquired using the circumferential ITP array. Previous work [15] suggested the possibility of propagation of the first azimuthal duct mode, $(m,n) = (\pm 1, 0)$, where m and n denote azimuthal- and radial-mode orders, respectively. The mode-order index n indicates the number of pressure nodes (zeroes) in the radial profile. Table 2, adopted from Boyle et al. [15, Table A 2], displays estimated duct-mode cut-on/off frequencies for various power settings. Boyle et al. [15] used mean-line conditions, such as the local Mach number and speed of sound, from an engine-deck simulation for the DGEN 380 turbofan to determine the physical frequencies. The plane-wave mode (0,0) can always propagate. Of note is the fact that the cut-on/off frequencies for all radial mode orders, $n > 0$, are well outside of the range of interest from a combustor-noise perspective. The relatively small ratio of the annular-duct height to its outer radius (= 0.195) is the reason for the high radial-mode cut-on/off frequencies. In fact, modes with $\pm m$ = 1–14 are successively cut on before the first radial mode (0,1) is cut on [15]. Based on the information in Table 2, it follows that from a combustor-noise perspective (i.e. for frequencies up to about 1,600 Hz) only the first three azimuthal mode pairs, $(\pm 1, 0)$, $(\pm 2, 0)$, and $(\pm 3, 0)$, in addition to the always cut-on plane wave mode $(0, 0)$, need to be resolved, which is within the capability of the present circumferential ITP array.

Among others, modal decomposition using circumferential sensor arrays have been performed by Karchmer [22], Schuster and Mendoza [23], and Royalty and Schuster [6]. Karchmer [22] assumed standing waves in the azimuthal direction, i.e. equal amplitudes of the modes in each $\pm m$ pair, and solved for the amplitudes in a least-square sense. This approach has also been used by Krejsa and Karchmer [24] and Miles [25]. However, Schuster and Mendoza [23] and Royalty and Schuster [6] did not make the standing wave assumption and obtained the mode contributions by direct application of the discrete Fourier transform (DFT) in both the circumferential direction and time. This latter approach is followed herein. The modal decomposition will be illustrated for the 60% power setting, which is taken as a suitable representation of approach conditions where combustor noise is often prominent in practice.

Auto-Spectra, Coherence, and Phase Lag. As a preparation for the modal decomposition, it is instructive to examine the auto-spectra of the sensor signals as well as the coherence and phase lag between the signals. For the latter two, the NE801 sensor provides the reference signal. Figure 16 shows the *SPL* (i.e.normalized

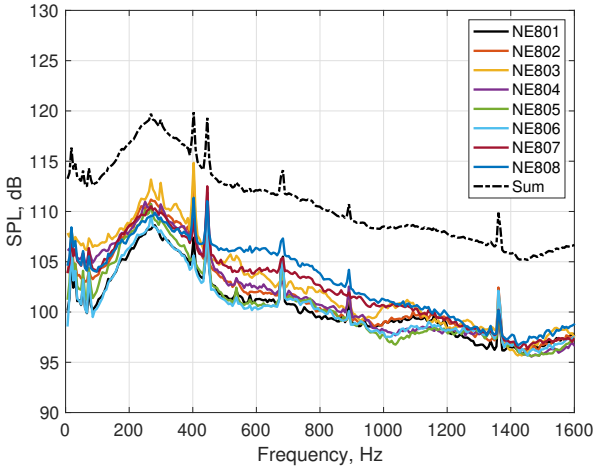

Fig. 16 Circular-array auto-spectra (*SPL*) for 60% N_{Lc} power setting; clocked array orientation

auto-spectra in dB) for the eight sensors NE801–NE808 as well as their mean-pressure-squared sum for frequencies up to 1,600 Hz at 60% power and clocked array orientation. The dot-dashed line denoting the *SPL* sum, can be interpreted as the averaged *SPL* spectra shifted up by $10\log_{10}(8)$ dB (≈ 9 dB).

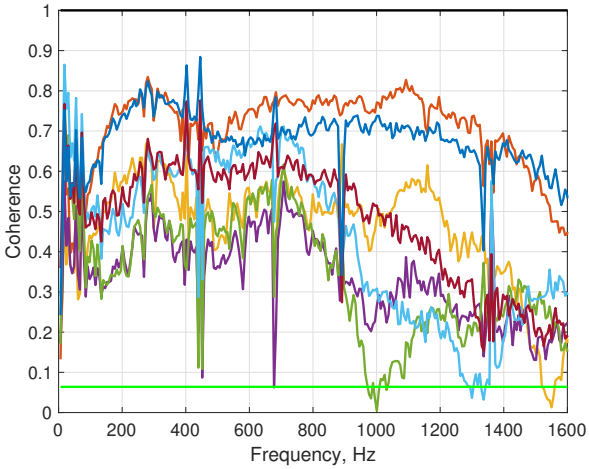

Fig. 17 Circular-array sensor-signal coherence at 60% N_{Lc} power setting; reference sensor: NE801; clocked array orientation; same legend as Fig. 16; horizontal bright green line: 95% confidence limit

Figure 17 shows the sensor-signal coherence with NE801 as reference sensor for frequencies less than 1,600 Hz, 60% power, and clocked array orientation. The coherence of two signals is given by the magnitude (absolute value) of their cross-spectrum normalized

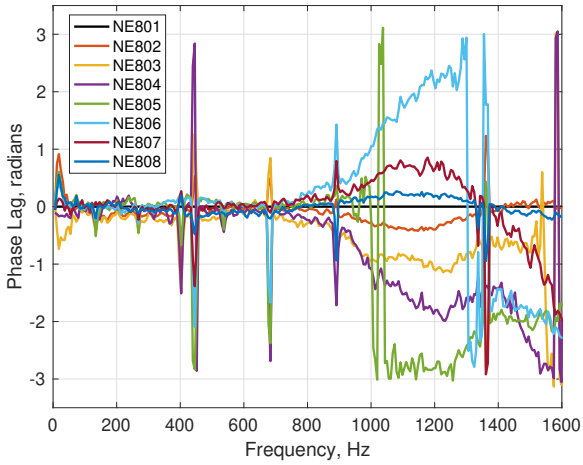

Fig. 18 Circular-array sensor-signal phase lag at 60% N_{Lc} power setting; reference sensor: NE801; clocked array orientation

by the square root of the product of their auto-spectra. Theoretically, the coherence ranges from zero to unity, with the values zero and unity indicating no dependency and perfect linear dependency between the signals, respectively. In practice, since the time series are finite, zero coherence can not be achieved. Instead, a statistical measure can be used to judge if the signals are independent. The horizontal bright green line in this figure indicates a 95%-probability threshold value. If the computed coherence is less than this value, the two signals are considered independent. The results shown indicate statistically significant coherence for all signal pairs over most of the frequency range of interest from a combustor-noise point of view.

The cross-spectrum between two signals is a complex quantity. Its magnitude was used above in the determination of their coherence. The cross-spectrum phase simply describes the phase lag between the two signals. Figure 18 presents the phase lag of the sensor signals with respect to the NE801 signal. The rapid variations in the phase lag seen in regions where the coherence is very low are not physical, but simply a reflection of the inherent difficulty, or uncertainty, in computing a phase value under such conditions, and should be disregarded. Keeping this in mind, the phase relationships are, generally, well behaved and close to zero below the first cut-on/off frequency in Table 2, which is just under 800 Hz. Beyond that frequency, the phase lag initially increases asymmetrically for sensor pairs (NE802/NE808, NE803/NE807, and NE804/NE806) that are at the same circumferential distance from the reference sensor, but this asymmetry starts to break down around 900 Hz.

Modal-Decomposition Procedure. Consider the M time series, each containing N sample points,

$$u_n^{(l)} = u(\theta_n, t^{(l)}), \quad l = 0, 1, \ldots, M-1, \tag{2}$$

where $\theta_n = 2\pi n/M$, $n = 0, 1, \ldots, M-1$, are the circumferential sensor locations, $t^{(l)} = l/f_s$, $l = 0, 1, \ldots, N-1$ are times of the sample points, and f_s is the sampling rate. The DFT with respect to time of each sensor signal can be written as

$$U_n^{(k)} = \sum_{l=0}^{N-1} u_n^{(l)} e^{i2\pi kl/N}, \quad k = 0, 1, \ldots, N-1, \tag{3}$$

for each value of n. The superscript k is a frequency index, with the associated frequency given by $f^{(k)} = k f_s/N$. The corresponding inverse DFT is

$$u_n^{(l)} = \frac{1}{N} \sum_{k=0}^{N-1} U_n^{(k)} e^{-i2\pi kl/N}, \quad l = 0, 1, \ldots, N-1. \tag{4}$$

The DFT with respect to the azimuthal coordinate, θ, can be defined through

$$a_m^{(l)} = \sum_{n=0}^{M-1} u_n^{(l)} e^{-i2\pi mn/M}, \quad m = 0, 1, \ldots, M-1, \tag{5}$$

for each value of l. The index m represents the azimuthal wave number. The inverse given by

$$u_n^{(l)} = \frac{1}{M} \sum_{m=0}^{M-1} a_m^{(l)} e^{i2\pi mn/M}, \quad n = 0, 1, \ldots, M-1. \tag{6}$$

Using Eqs. (3)–(6) produces the forward and inverse double DFT pair

$$A_m^{(k)} = \sum_{l=0}^{N-1} \sum_{n=0}^{M-1} u_n^{(l)} e^{-i2\pi(mn/M - kl/N)}, \tag{7}$$

$$u_n^{(l)} = \frac{1}{MN} \sum_{k=0}^{N-1} \sum_{m=0}^{M-1} A_m^{(k)} e^{i2\pi(mn/M - kl/N)}. \tag{8}$$

Note that the opposite sign in the exponent is used in the azimuthal DFT compared to the time DFT. This means that a positive value of m corresponds to a wave traveling in the positive azimuthal direction.

It is relatively straightforward to show that

$$\sum_{n=0}^{N-1} |U_n^{(k)}|^2 = \frac{1}{M} \sum_{m=0}^{M-1} |A_m^{(k)}|^2, \tag{9}$$

for all k, i.e. frequencies. This relation is just another manifestation of Parseval's identity. Since $|U_n^{(k)}|^2$ represents the two-sided auto-spectrum of the signal u_n, it follows that $|A_m^{(k)}|^2/M$ is the auto-spectrum associated with the mode m.

The actual decomposition procedure generally followed Schuster and colleagues [6, 23]. For each time step, the azimuthal DFT, Eq. (5), was applied to the sensor-array data producing discrete time series for the modal amplitudes $a_m^{(l)}$. Second, the MATLAB routine `cpsd` was used to compute the auto-spectra for each mode. Hamming windowing and 50% segment overlap was used. The results were renormalized (by M) in view of Eq. (9) and converted to one-sided spectra. Note that since the azimuthal DFT coefficients are cyclic, i.e. $a_{M+m}^{(l)} = a_m^{(l)}$, it follows that the spectra with the indexes $m = 1, 2, \ldots, M/2$ correspond to positive wave numbers in the usual sense and that the remaining spectra correspond to negative wave numbers through the reassignment $M-m \rightarrow -m$ for $m = 1, 2, \ldots, M/2-1$. Consequently, the modal-decomposition technique covers the $m = 0$ (plane wave), $\pm1, \pm2, \pm3$, and $+4$ modes for the present array.

Modal-Decomposition Results. Figure 19 shows the modal decomposition of the *SPL* at the circumferential-array location as well as their mean-pressure-squared sum for frequencies up to 1,600 Hz at 60% power and clocked array orientation. The dot-dashed curve denoting the *SPL* sum matches the corresponding result in Fig. 16 as implied by Eq. (9). The plane-wave mode clearly dominates at low frequencies up to about the estimated cut-on/off frequency (just under 800 Hz) for the first azimuthal modes and is

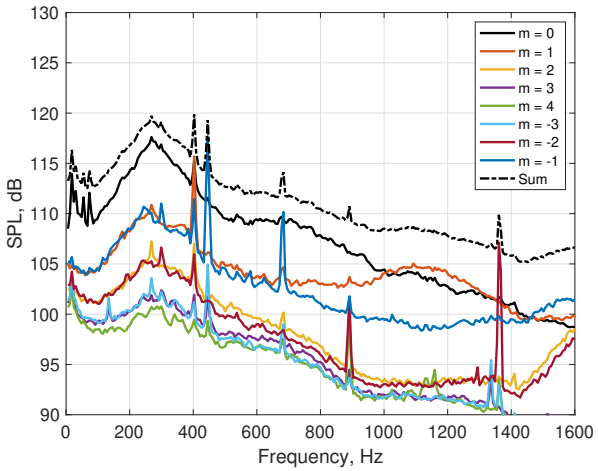

Fig. 19 Modal contributions to the *SPL* at the core-nozzle exit at 60% N_{Lc} power setting; clocked array orientation

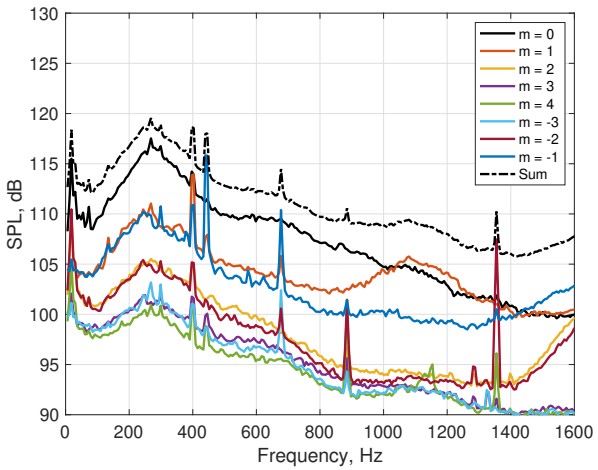

Fig. 20 Modal contributions to the *SPL* at the core-nozzle exit at 60% N_{Lc} power setting; standard array orientation

overtaken by the $m = 1$ mode at about 1 kHz. Somewhat unexpectedly, the $m = 1$ mode contribution significantly exceeds that of the $m = -1$ mode over a significant frequency range, especially after the point where the plane-wave mode loses its dominance, with the largest ±1-mode difference occurring around 1,100 Hz. This could possibly be explained by the fact that a positive-m mode rotates in the same direction as the low-pressure-spool shaft and hence there could be some residual swirl, i.e. a bulk rotation, in the flow at this location. Schuster and Mendoza [23], in their study of auxiliary-power-unit combustors, suggested this as a reason for their observed difference in peak frequencies for positive and negative azimuthal modes. However, they found that the peak-frequency separation increased with mode order. In contrast, here the amplitude difference for each of the $m = \pm 2$ and $m = \pm 3$ pairs are not as stark as for the $m = \pm 1$ pair.[10] Consequently, the observed $m = \pm 1$ behavior remains an unexplained mystery. An assumption about equal modal amplitudes for positive and negative azimuthal-wave-number pairs may approximately be valid for the ±2 and ±3 modes, but it doesn't appear that such an assumption holds for the $m = \pm 1$ pair.

The $m = \pm 2$ modes are estimated, see Table 2, to cut on at a value just under 1,600 Hz and their *SPL* contributions catch up with the plane-wave mode at about that frequency. This trend was also observed for $m = \pm 3$ modes, but their cut-on frequency is outside of the frequency range illustrated in this figure, however. Various tones and their harmonics are also captured in the individual modal *SPL* spectra.

The reason for having two configurations for the circumferential array (standard and clocked) is that there are six support struts traversing the core nozzle near its exit. The struts are located in the 2, 4, . . . , and 12 o'clock circumferential positions. Consequently, in the standard-array orientation, two of the ITP ports (NE801 and NE805) are directly downstream of struts. In the clocked configuration, no pressure ports are directly downstream of a strut. This is also the motivation for first having discussed the clocked case in this section.

Figure 20 shows the same information as Fig. 19, but now for the standard array orientation. The overall features of the modal decomposition for the two configurations are generally the same. The broadband *SPL* values, both circumferentially-overall (dot-dashed) and for individual modes, are essentially the same for the lower frequencies, but start to deviate slightly at the higher frequencies. The circumferential-overall *SPL* spectra are both dominated by the plane-wave mode contribution for frequencies below the estimated cut-on value for the ±1 modes. The modal content and cut-on indicators are largely unchanged between the two cases. Since, levels and trends are very similar, if not nearly identical, for the two configurations, it can be concluded that the array orientation had no significant impact on the modal decomposition results.

[10]The frequency ranges where the $m = \pm 2$ and $m = \pm 3$ modes dominate are not included in Fig. 19

Summary and Conclusions

An analysis of acoustic data from a core/combustor-noise source-diagnostic test using the DGEN Aeropropulsion Research Turbofan resource at the NASA Glenn Research Center is presented. The test took place within the anechoic Aero-Acoustic Propulsion Laboratory and involved extensive acoustic instrumentation. A microphone array in the geometric farfield, two alternate sideline microphone arrays, and a circumferential array of unsteady-pressure sensors at the core-nozzle exit were deployed. Typically, 93 channels of high-data-rate acoustic measurements were simultaneously acquired at each test point. The test campaign was undertaken with a goal of further the understanding of sources, and propagation to the farfield, of significant core-noise components. The ultimate goal was to enable improved prediction and mitigation techniques for propulsion noise through better physical understanding as well as the development of a high-quality database of relevant acoustic data for tool development.

A data-quality survey of the acoustic measurements determined that the acquired data can serve as a solid basis for further analytical and experimental work.

Furthermore, previous work [15] had given indications that the ±1 azimuthal duct mode was present at the core-nozzle exit and could propagate core/combustor noise to the farfield. This was an impetus, among other, to determine any modal content beyond the plane-wave component, in the low frequency range of interest to core/combustor noise, through proper instrumentation in the core nozzle. A circumferential array of eight unsteady pressure sensors, in an infinite-tube-probe arrangement, was employed for this purpose. It was implemented through the use of a modified engine tailcone, which provides the inner wall of the annular core duct near the exit. The modal-decomposition analysis performed here, using the circumferential-array data, confirmed the presence of ±1 as well as ±2 and ±3 azimuthal modes at the core nozzle exit. At low frequencies the plane-wave mode is dominant. As expected, the azimuthal duct modes started to successively become dominant at frequencies consistent with their estimated cut-on/off values. The ±2 and ±3 azimuthal-mode pairs showed clear characteristics of being standing waves in the circumferential direction. However, the +1 component, which rotates in the same direction as the low-pressure-spool shaft, clearly had a larger amplitude than the

−1 component once the estimated cut-on frequency was exceeded. The reason for this different behavior is not clear at present.

The current work represents a solid foundation/precursor for the application of recent advanced source-separation methods, that combine coherence and mode-decomposition techniques (eg. Davies and Bennett [11]). The processing of the current data set using such methods is in underway, with the results to be reported in a future publication. This ongoing work is expected to illuminate the impact of the core-noise modal structure at the nozzle exit on the farfield noise signature, which is an essential aspect of the development of better turbofan noise-prediction methods.

Until much more is known of the specific details and characteristics of far-term combustors, it is hard to point to, or suggest, a particular technique that would be most effective in reducing noise for future combustor designs. However, it is clear that broadband acoustics (and not just thermo-acoustic instability-considerations) needs to be an integral part of the early design stages for far-term combustor concepts. To not do so introduces a significant risk of setting long-term combustor technology directions which unnecessarily compromise community-noise impact.

The development of lightweight, high-temperature, low-frequency broadband acoustic treatments is an avenue of research with both near- and far-term importance for core/combustor-noise mitigation. The combination of the long wavelengths involved and the limited space available in the engine hot sections (core and core nozzle) represents a significant challenge for the designers. Research and realistic-environment testing in support of such development efforts are needed.

Plans are underway for more invasive instrumentation of the small turbofan engine used here, eventually culminating in direct observations within the combustor. Additionally, the development of high-temperature acoustic treatments to be tested using this resource is under consideration. The current results will allow the designers to precisely target the acoustic field present at the core-nozzle exit.

Acknowledgments

This work is supported by the NASA Advanced Air Vehicles Program, Advanced Air Transport Technology Project. Trade names and trademarks are used in this report for identification only. Their usage does not constitute an official endorsement, either expressed or implied, by the National Aeronautics and Space Administration.

References

[1] Mongeau, L., Huff, D., and Tester, B. J., 2013, "Aircraft Noise Technology Review and Medium and Long Term Noise Reduction Goals," *ICA 2013 Montreal*, Proc. Mtgs. Acoust. 19, 040041, doi: 10.1121/1.4800944.

[2] Tam, C. K. W., Bake, F., Hultgren, L. S., and Poinsot, T., 2019, "Combustion Noise: Modeling and Prediction," CEAS Aeronautical J., **10**(1), pp. 101–122.

[3] Mendoza, J. M., Nance, D. K., and Ahuja, K. K., 2008, "Source Separation from Multiple Microphone Measurements in the Far Field of a Full Scale Aero Engine," AIAA Paper 2008-2809, 14th AIAA/CEAS Aeroacoustic Conference, Vancouver, British Columbia, doi: 10.2514/6.2008-2809.

[4] Hultgren, L. S. and Miles, J. H., 2009, "Noise-Source Separation Using Internal and Far-Field Sensors for a Full-Scale Turbofan Engine," AIAA Paper 2009-3220 (NASA/TM–2009-215834), 15th AIAA/CEAS Aeroacoustic Conference, Miami, Florida, doi: 10.2514/6.2009-3220.

[5] Weir, D. S., 2008, "Engine Validation of Noise and Emission Reduction Technology Phase I," Tech. Rep. NASA/CR-2008-215225, NASA, Honeywell Report No. 21-13843, Honeywell Aerospace, Phoenix, Arizona.

[6] Royalty, C. M. and Schuster, B., 2008, "Noise from a Turbofan Engine Without a Fan from the Engine Validation of Noise and Emission Reduction Technology (EVNERT) Program," AIAA Paper 2008-2810, 14th AIAA/CEAS Aeroacoustics Conference, Vancouver, British Columbia, doi: 10.2514/6.2008-2810.

[7] Miles, J. H., 2009, "Time Delay Analysis of Turbofan Engine Direct and Indirect Combustion Noise Sources," J. Propulsion and Power, **25**(1), pp. 218–227.

[8] Hultgren, L. S., 2011, "Full-Scale Turbofan-Engine Turbine-Transfer Function Determination Using Three Internal Sensors," AIAA Paper 2011-2912 (NASA/TM-2012-217252), 17th AIAA/CEAS Aeroacoustic Conference, Portland, Oregon, doi: 10.2514/6.2011-2912.

[9] Harper-Bourne, M., Moore, A., and Siller, H., 2008, "A Study of Large Aero-Engine Combustor Noise," AIAA Paper 2008-2942, 14th AIAA/CEAS Aeroacoustic Conference, Vancouver, British Columbia, doi: 10.2514/6.2008-2942.

[10] Pardowitz, B., Tapken, U., Knobloch, K., Bake, F., Bouty, E., Davis, I., and Bennett, G., 2014, "Core Noise — Identification of Broadband Noise Sources of a Turbo-Shaft Engine," AIAA Paper 2014-3321, 20th AIAA/CEAS Aeroacoustics Conference, Atlanta, Georgia, doi: 10.2514/6.2014-3321.

[11] Davis, I. and Bennett, G. J., 2011, "Spatial Noise Source Identification of Tonal Noise in Turbomachinery Using the Coherence Function on a Modal Basis," AIAA Paper 2011-2825, 17th AIAA/CEAS Aeroacoustic Conference, Portland, Oregon, doi: 10.2514/6.2011-2825.

[12] Schuster, B., Gordon, G., and Hultgren, L. S., 2015, "Dynamic Temperature and Pressure Measurements in the Core of a Propulsion Engine," AIAA Paper 2015-2819, 21st AIAA/CEAS Aeroacoustic Conference, Dallas, Texas, doi: 10.2514/6.2015-2819.

[13] Gordon, G., 2015, "Acoustic Database for Turbofan Engine Core-Noise Sources, Volume I—Final Report," Tech. Rep. NASA/CR–2015-218879/VOL1, NASA, Honeywell Report No. 21-15066(10), Honeywell Aerospace, Phoenix, Arizona.

[14] Tam, C. K. W., Li, Z., and Schuster, B., 2016, "An Investigation on Indirect Combustion Noise Generation in a Turbofan Engine," AIAA Paper 2016-2746, 22nd AIAA/CEAS Aeroacoustic Conference, Lyon, France, doi: 10.2514/6.2016-2746.

[15] Boyle, D. K., Henderson, B. S., and Hultgren, L. S., 2018, "Core/Combustor-Noise Baseline Measurements for the DGEN Aeropropulsion Research Turbofan," AIAA Paper 2018-3281, 24th AIAA/CEAS Aeroacoustics Conference, Atlanta, Georgia, doi: 10.2514/6.2018-3281.

[16] Iberall, A. S., 1950, "Attenuation of Oscillatory Pressures in Instrument Lines," J. Research National Bureau Standards, **45**, pp. 85–108.

[17] Bergh, H. and Tijdeman, H., 1965, "Theoretical and Experimental Results for the Dynamic Response of Pressure Measuring Systems," Tech. Rep. NLR-TR-F.238, Netherlands Aerospace Center (NLR).

[18] Karchmer, A. M. and Reshotko, M., 1976, "Core Noise Source Diagnostics on a Turbofan Engine Using Correlation and Coherence Techniques," Tech. Rep. NASA-TM-X-73535, NASA.

[19] Boyle, D. K., Henderson, B. S., and Hultgren, L. S., 2019, "Transfer-Function Determination for Infinite-Tube-Probe Pressure Transducers with Application to Turbofan Core/Combustor Noise," AIAA Paper 2019-2588 (NASA/TM–2019-220045), 25th AIAA/CEAS Aeroacoustics Conference, Delft, The Netherlands, doi: 10.2514/6.2019-2588.

[20] Hultgren, L. S., 2015, "A First Look at the DGEN380 Engine Acoustic Data From a Core-Noise Perspective," Tech. Rep. NASA/TM–2015-218924, NASA.

[21] Sutliff, D. L., Brown, C. A., Bayon, B., and Sree, D., 2016, "Farfield Acoustic Characteristics of the DGEN380 Turbofan Engine as Measured in the NASA Glenn Aero-Acoustic Propulsion Laboratory," AIAA Paper 2016-3006, 22nd AIAA/CEAS Aeroacoustic Conference, Lyon, France, doi: 10.2514/6.2016-3006.

[22] Karchmer, A. M., 1983, "Acoustic Modal Analysis of a Full Scale Annular Combustor," AIAA Paper 1983-0760 (NASA-TM-83334), 8th AIAA Aeroacoustics Conference, Atlanta, Georgia, doi: 10.2514/6.1983-760.

[23] Schuster, B. and Mendoza, J. M., 2007, "Auxiliary Power Unit Combustion Noise Mesurements," Paper 2, X3-NOISE Scientific Workshop, 27–28 September, Lisbon, Portugal.

[24] Krejsa, E. A. and Karchmer, A. M., 1983, "Acoustic Modal Analysis of the Pressure Field in the Tailpipe of a Turbofan Engine," Tech. Rep. NASA-TM-83387, NASA.

[25] Miles, J. H., 2007, "Restricted Modal Analysis Applied to Internal Annular Combustor Autosoectra and Cross-Spectra Measurements," AIAA J., **45**(5), pp. 988–999.

List of Figures

List of Tables